Stratospheric Age-of-Air: Sensitivity to Finite Volume Remapping Algorithm

Clara Orbe[1,2], Lawrence L. Takacs[3,4], Amal El Akkraoui[3,4],
Krzysztof Wargan[3,4], Andrea Molod[3], William Putman[3], Steven Pawson[3]

[1]NASA Goddard Institute for Space Studies, New York, NY
[2]Department of Applied Physics and Applied Mathematics, Columbia University, New York, NY
[3]Global Modeling and Assimilation Office, NASA Goddard Space Flight Center, Greenbelt, MD
[4]Science Systems and Applications, Inc., Lanham, MD, USA

Key Points:

- The stratospheric mean age-of-air simulated in GEOS is sensitive to the remapping scheme used within the finite-volume dynamical core.
- This sensitivity in the age-of-air is significant ($\sim$30%) and imprints on the simulated distributions of several long-lived chemical trace gases, including nitrous oxide and methane.
- The age-of-air sensitivities primarily reflect changes in resolved wave convergence over the Northern Hemisphere midlatitude stratosphere, which impact mean upwelling in the tropical lower stratosphere.

Corresponding author: Clara Orbe, `clara.orbe@nasa.gov`

Abstract

Accurately modeling the large-scale transport of trace gases and aerosols is critical for interpreting past (and projecting future) changes in atmospheric composition. Simulations of the stratospheric mean age-of-air continue to show persistent biases in chemistry climate models, although the drivers of these biases are not well understood. Here we identify one driver of simulated stratospheric transport differences among various NASA Global Earth Observing System (GEOS) candidate model versions under consideration for the upcoming GEOS Retrospective analysis for the 21st Century (GEOS-R21C). In particular, we show that the simulated age-of-air values are sensitive to the so-called "remapping" algorithm used within the finite-volume dynamical core, which controls how individual material surfaces are vertically interpolated back to standard pressure levels after each horizontal advection time step. Differences in the age-of-air resulting from changes within the remapping algorithm approach ~ 1 year over the high latitude middle stratosphere - or about 30% climatological mean values – and imprint on several trace gases, including methane (CH_4) and nitrous oxide (N_2O). These transport sensitivities reflect, to first order, changes in the strength of tropical upwelling in the lower stratosphere (70-100 hPa) which are driven by changes in resolved wave convergence over northern mid-latitudes as (critical lines of) wave propagation shift in latitude. Our results strongly support continued examination of the role of numerics in contributing to transport biases in composition modeling.

Plain Language Summary

Large-scale transport plays a crucial role in distributing climatically important trace constituents in the atmosphere, especially in the stratosphere where transport largely determines the chemical lifetimes of trace gases. One summary of transport in the stratosphere is the "mean age" or the mean transit time since air at a point in the stratosphere was last in the troposphere. Current models used for simulating stratospheric composition produce a range of simulated ages, although these differences are poorly understood. Among other factors, model numerics play a critical role in transport, but few studies have explored the sensitivity of the mean age to the choice of numerical scheme employed within different dynamical cores. Here we use one model to show that the mean age is sensitive to the so-called "remapping" algorithm used within the finite-volume dynamical core that controls how individual material surfaces are vertically interpolated back to standard pressure levels after each horizontal advection time step. This reflects sensitivities in the representation of how waves propagate from the troposphere into the stratosphere. This work suggests that model numerics can be an important factor in contributing to differences in simulated transport among models.

1 Introduction

The chemical and radiative properties of the troposphere and lower stratosphere are strongly influenced by the stratosphere-troposphere exchange of mass and tracers (e.g., Morgenstern and Carver (2001); Hegglin et al. (2006); Pan et al. (2007)). Properly simulating the stratospheric circulation and its influence on atmospheric composition in earth system models is important for capturing past decadal trends in surface climate, particularly in response to changes in Southern Hemisphere ozone depletion (e.g., Son et al. (2009); Polvani et al. (2011)). In the Northern Hemisphere (NH), the stratospheric circulation's coupling to ozone could represent an important feedback on the climate's response to future increases in greenhouse gases (GHGs), especially over the North Atlantic (e.g., Chiodo and Polvani (2019)). On shorter subseasonal timescales, stratospheric ozone changes associated with strong polar vortex states may also modulate Arctic sea level pressure and surface temperatures (e.g., Ivy et al. (2017); Oehrlein et al. (2020)), so much so that seasonal forecast systems employing prognostic ozone show suggestions

of increased signal-to-noise ratio in predictions of the North Atlantic Oscillation (B. M. Monge-Sanz et al. (2022)).

Key to accurately simulating a consistent representation of coupling between stratospheric dynamics and chemical trace gases is ensuring that a model's underlying transport circulation is properly represented. To this end, much effort has been paid to developing and refining so-called "tracer-independent" metrics of transport (Holzer and Hall (2000)) such as the mean age-of-air (Hall and Plumb (1994)) and to applying these measures to rigorously evaluate model transport characteristics in chemistry climate models (CCMs) (e.g., Hall et al. (1999); Orbe et al. (2018); Dietmüller et al. (2018); Abalos et al. (2020)).

While the assessment of CCMs participating in the SPARC Chemistry Climate Model Validation (SPARC CCMVal) effort showed a marked improvement in simulated transport characteristics relative to previous intercomparisons (J. Neu et al. (2010)), more recent analysis of models participating in the SPARC Chemistry Climate Modeling Initiative (CCMI) (Eyring et al. (2013)) do not demonstrate any improvement (Dietmüller et al. (2018), see their Figure 3). In particular, although some models produce mean age values that agree well with observational estimates, the CCMI intermodel spread is $\sim$ 50%, with models generally simulating transport that is too vigorous relative to observations. While documenting these transport differences among models is straightforward, understanding the drivers of this spread remains a key challenge and there is still no consensus on what is causing the large spread in simulated ages among the current generation of CCMs.

A key challenge in identifying the drivers of age-of-air – and other stratospheric transport – biases is that they reflect the time-integrated effects of advection by the residual mean circulation and eddy diffusive mixing, or the quasi-random transport due to the breaking of Rossby waves (e.g., Holton et al. (1995); Plumb (2002)). Given that the influences of mixing and advection are not easily separable, studies have come to different conclusions about sources of age biases in models. In particular, the analysis of the CCMVal models showed a strong correlation between the intermodel spread in the age-of-air and lower stratospheric tropical upwelling, whereas Dietmüller et al. (2018) showed that the age spread among the CCMI models was driven by differences in mixing. While future attempts to further distinguish between sources of age biases using either simplified "leaky pipe" models (Plumb (1996); J. L. Neu and Plumb (1999)) or more complete measures of the transport circulation such as the "age spectrum" (e.g., Hall and Plumb (1994); Waugh and Hall (2002))) may prove enlightening, at present there is no consensus on what is causing large simulated age-of-air biases in models.

One potential limitation of previous work based on multi-model intercomparisons is that many aspects of model formulation can influence both stratospheric upwelling and mixing. Thus, while intercomparisons are useful for identifying common model biases, understanding the drivers of these biases is difficult absent single model-based process studies. Among these, several aspects of model formulation have been identified as influencing simulated mean age distributions. As the mean age is sensitive to vertical motion in the lowermost stratosphere, these include large sensitivities to vertical resolution (Orbe et al. (2020)) and to spurious vertical mixing either introduced in vertical coordinate transformations in offline chemical transport models (B. Monge-Sanz et al. (2007)) or through use of assimilated winds performed either in offline (e.g., Legras et al. (2004)) or online data assimilation and "nudged" configurations (e.g., Pawson et al. (2007); Orbe et al. (2017); Davis et al. (2022)). These age sensitivities can be still further amplified, depending on whether or not parameterized gravity waves are included (Eichinger et al. (2020)).

By comparison, sensitivities of the mean age to underlying tracer numerics have been less well examined, although Eluszkiewicz et al. (2000) documented a large sensi-

tivity in simulated age-of-air values to the choice of advection scheme. More recently, Gupta et al. (2020) showed differences of $\sim 25\%$ in the age-of-air across identical experiments performed using four different dynamical cores, especially between those using spectral versus finite-volume schemes. The experiments employed in that study, however, were highly idealized and it is not clear if the strong influence of tracer numerics that they identified is also realized in more comprehensive model simulations with moist physics, especially in the context of model development as carried out in operational modeling centers.

To better elucidate this influence of tracer numerics on the transport properties simulated in a comprehensive global model context, here we document the sensitivity of the stratospheric mean age in several recent versions of the NASA Global Earth Observing System (GEOS) general circulation model (Molod et al., 2015) that represent different stages in model development since the Modern-Era Retrospective Analysis for Research and Applications Version 2 (MERRA-2; Gelaro et al. (2017)).

Our focus on transport evaluation is in wake of the upcoming release of the GEOS Retrospective analysis for the early 21st Century (GEOS-R21C), which will serve as an intermediate atmospheric reanalysis between MERRA-2 and the future coupled atmosphere-ocean reanalysis MERRA-3 (in-preparation). As part of the current effort to explore coupling of more Earth System components targeting MERRA-3, GEOS-R21C will be used to drive an off-line chemistry reanalysis R21C-Chem with a full chemistry model (GEOS-Chem) and an advanced Constituent Data Assimilation component to update the chemistry fields. Since R21C-Chem will be produced in replay-mode (one-way coupling) whereby the meteorology fields are used to define the background atmospheric flow (Orbe et al., 2017), it is imperative that GEOS-R21C produces a credible representation of transport processes.

In particular, here we document how in the process of evaluating candidate systems for GEOS-R21C we found that the mean age was ~ 1 year younger (or $\sim 30\%$ smaller) than the values simulated in the model version used to produce MERRA-2 (Figure 1). The model versions shown in Figure 1 reflect more than 10 years' worth of accumulated changes in model development, most notably changes in radiation, parameterized convection and, as we focus on here, changes in the algorithm used to transform advected fields from Lagrangian levels to the new pressure levels after each horizontal advection time step. This is the model's description of vertical advection. We show that slight modifications in this so-called "remapping" algorithm are the primary driver of the age-of-air changes exhibited in recent GEOS-R21C candidate model versions, a result which may have broader implications for other general circulation models using finite volume (FV) dynamical cores. We begin by discussing methods in Section 2 and present key results and conclusions in Sections 3 and 4, respectively.

2 Methods

2.1 Model Configurations

Here we present results from several versions of GEOS spanning MERRA-2 to more recent candidates for GEOS-R21C. Among these model versions, a subset are more "official" as they have been documented and/or employed in recent model intercomparisons and are highlighted in Figure 1. In particular, these include a model version that was used in Phase 1 of CCMI and documented in Orbe et al. (2017) (Fig. 1, red line). A more recent model tag that was used in the CCMI Phase 2 simulations (correspondence with Michael Manyin) is also shown (Fig. 1, green line).

We begin by comparing 10-year (2000-2010) climatological mean zonally averaged age-of-air profiles at 50 hPa across this subset of model versions, derived from 30-year long atmosphere-only (AMIP) integrations constrained with observed sea surface tem-

Mean Age-of-Air (Γ) at 50 hPa
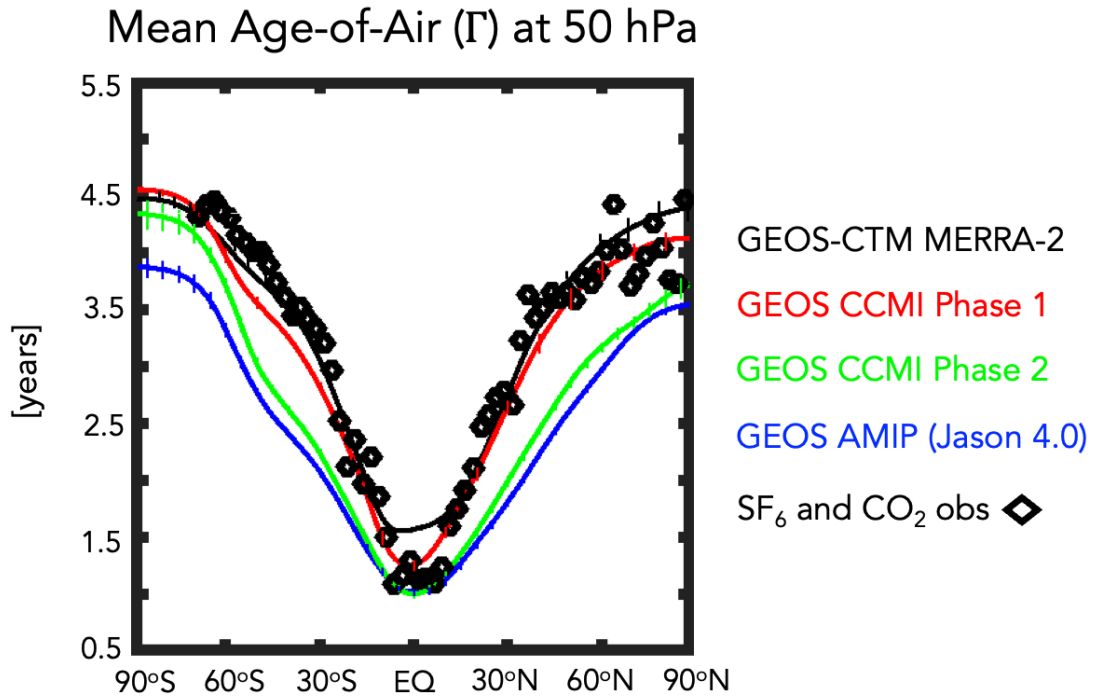
Figure 1. The 2000-2010 climatological annual mean meridional profile of the stratospheric mean age-of-air (Γ), evaluated at 50 hPa. Results from a GEOS-CTM integration constrained with MERRA-2 meteorological fields (black line) as well as free-running GEOS simulations using a model configuration for CCMI Phase 1 (red line), CCMI Phase 2 (green line) and a more recent GEOS-FP development tag (Jason 4.0, blue line) are shown. All simulations are constrained with the same (observed) historical sea surface temperatures. Diamonds correspond to SF_6 and CO_2 in situ based estimates of Γ from Boering et al. (1996) and Engel et al. (2009). Vertical dashed lines denote $\pm\sigma$, the standard deviation of Γ over 2000-2010, for each model simulation.

peratures (Figure 1). First, we note that the profiles for the CCMI Phase 1 version of the model are very close to observations (black stars), consistent with the "GEOSCCM" documented age characteristics reported in Dietmüller et al. (2018) (see their Figure 3). In addition, while passive tracers were not integrated within MERRA-2, results using the GEOS chemistry transport model (GEOS-CTM, Kouatchou et al. (2015)) constrained with MERRA-2 meteorological fields (black line) also exhibits good agreement with observed values. This good agreement between the CTM-generated age-of-air and the observations is consistent with results from a previous GEOS-CTM simulation (constrained with MERRA) as documented in Orbe et al. (2017).

Moving to more recent development versions of the model (green and blue lines), however, reveals a reduction in the mean age by ~ 1 year over both southern and northern high extratropical latitudes, or a decrease of $\sim 20\text{-}30\%$ relative to the MERRA-2 constrained simulation and the observations. As discussed earlier, the green line refers to the CCMI Phase 2 model version, whereas the blue line refers to an undocumented candidate version (model tag Jason 4.0) that corresponds best to a model configuration similar to what is used in the GEOS forward processing (FP) numerical weather prediction system. Note that this decrease in the climatological age in both model versions far exceeds the (internal) variations in mean age that occur interannually (vertical bars on solid lines).

There are numerous development updates in the model that have occurred since MERRA-2. Therefore, after discussing the model configurations highlighted in Figure 1 in Section 3.1, we then present results from targeted experiments aimed at successively undoing these changes one-by-one (Section 3.2). Among those aspects most relevant to the stratospheric transport circulation, we first present results from experiments which undo recent changes in the radiation scheme, which was updated from Chou and Suarez (1994) in the shortwave and Chou (1990, 1992) in the longwave to the Rapid Radiative Transfer Model for GCMS (RRTMG; Iacono et al. (2008).

xr

After addressing the radiation changes, we focus on a still more consequential update that was made to the handling of the remapping algorithm within the model's FV dynamical core (Lin, 2004). Within the FV core vertical motion is realized through the Lagrangian transport of the "floating" vertical coordinate such that after each horizontal advection step the individual material surfaces are vertically interpolated back to the model's new pressure levels through FV's so-called "REMAP" algorithm. This is needed because the Lagrangian surfaces that vertically bound the finite volumes will eventually deform, negatively impacting the accuracy of the horizontal-to-Lagrangian-surface transport and the computation of the pressure-gradient terms.

Since MERRA-2 several changes were made to the remapping algorithm. In its current implementation the algorithm involves 1) fitting piecewise parabolic (hereafter PPM) functions to input layer-mean values of T, U, V, Q and tracers; 2) calculating PPM functions to output layer edges; and 3) integrating PPM functions between output layer edges to produce new layer-mean values of T, U, V, Q and tracers. Note that T, U, V, Q, C_p, K and Φ correspond to temperature, zonal wind, meridional wind, specific humidity, specific heat capacity and kinetic and potential energy, respectively. This implementation is consistent with what is currently being used in most recent GEOS model versions (i.e. blue and green lines, Figure 1) and hereafter is referred to as REMAP Option 2 (Table 1, left).

The alternative version – which best mimics what was used in MERRA-2 – involves two main changes to this procedure and is hereafter referred to as REMAP Option 1 (Table 1, right; red line in Figure 1). First steps 1) and 3) are performed only for U, V, Q and tracers (not T). Second, three additional steps after 3) are added, the first two of

Table 1. **Finite Volume Remapping Algorithm**: The two versions examined in this study control how individual material surfaces are vertically interpolated back to standard pressure levels. REMAP Options 2 and 1 corresponds to the configurations used in more recent (green and blue lines, Figure 1) and older (red and black lines, Figure 1) model configurations, respectively. Here T, U, V, Q, C_p, K and Φ correspond to temperature, zonal wind, meridional wind, specific humidity, specific heat of air at constant pressure and kinetic and potential energy, respectively.

Step	REMAP Option 2 (CTRL)	REMAP Option 1 (MERRA-2)
1	Fit PPM functions to input layer-mean T, U, V, Q and tracers	Fit PPM functions to input layer-mean U, V, Q and tracers
2	Calculate PPM to output layer edges	Calculate PPM to output layer edges
3	Integrate PPM functions between output layer edges to produce new layer-mean T, U, V, Q and tracers	Integrate PPM functions between output layer edges to produce new layer-mean U, V, Q and tracers
4	n/a	Calculate TE = C_pT + K + Φ at input mid-layer pressures
5	n/a	Calculate TE at output mid-layer pressures using cubic interpolation and a-posteriori integral conservation
6	n/a	Construct "remapped" T via T = (TE - K - Φ)/C_p

which involve calculating total energy (TE) at input mid-layer pressures and then performing cubic interpolation and a posteriori integral conservation at output mid-layer pressures. Finally, temperatures are "remapped" from total energy via T = (TE - K - Φ)/C_p.

When examining Table 1, it is important to note that Options 1 and 2 differ in two main respects. The most consequential difference involves the interpolation that occurs within step 5 in REMAP Option 1. By comparison, the use of TE (as opposed to T), is less consequential and has no major impact on the circulation (Appendix Figure A1a). To this end, the sensitivity experiments discussed in the next section mainly focus on identifying the age-of-air sensitivites to changes in the interpolation scheme used in REMAP Option 1, not to the change from the use of TE to T.

Finally, it is worth noting other important model development changes that occurred, particularly those related to the parameterization of deep convection (Grell and Freitas (2014); Freitas et al. (2018)), could directly impact the stratospheric circulation by influencing wave generation in the troposphere. Although these changes have had a substantial impact on the diurnal cycle of precipitation (Arnold et al. (2020)) and on convective transport within the troposphere (Freitas et al. (2020)), their influence on the large-scale stratospheric circulation is much smaller relative to the remapping and radiation changes.

2.2 Model Experiments

2.2.1 AMIP vs. EMIP

We begin our analysis by interpreting the results shown in Figure 1, which are all based on historical AMIPs that were performed at the same cubed sphere C180 (approximately half-degree) horizontal resolution. As they represent more official model versions

they serve as an important motivation for the experiments that follow. However, there are numerous (potentially compensating) development changes between these model versions which renders it nearly impossible to cleanly identify drivers of differences in their simulated transport.

To this end, in order to investigate the drivers of the differences in Figure 1 we perform targeted modeling experiments aimed at disentangling the influence of individual model development changes on stratospheric transport properties (Table 2). In order to evaluate impacts on transport climate statistics, we consider both a set of climatological AMIP (rows 1-4) as well as so-called "EMIP" (rows 5-7) experiments.

In particular, we carry out 30-year-long AMIP simulations at C180 resolution which we use to infer the climate characteristics of the different model configurations. The "EMIP" experiments – ensembles of 3-month-long integrations initialized on approximately November 15 of each year between 1985 and 2015 – are also used to infer impacts on simulated transport climate. As they are more computationally efficient than AMIPs since all 30 3-month integrations may be run in parallel, they are performed at both C180 and C360 resolutions in order to examine the sensitivity of our results to changes in horizontal resolution.

As shown in Appendix B, comparisons of the December-January-February (DJF) vertical profile of tropical upwelling show excellent agreement between EMIP and AMIP integrations carried out using the same model configuration (Appendix Figure B1). This somewhat incidental result represents, to the best of our knowledge, the first time that EMIP-based statistics have been shown to converge well to those from AMIPs for the stratospheric metrics considered in this study. This suggests that EMIPs, relative to AMIPs, may be used to provide a computationally more efficient initial assessment of the impacts of model changes on the stratospheric circulation.

2.2.2 Model Development Changes

Moving next to the precise model development changes examined, we begin by defining a control experiment (CTRL; Table 2, row 1), which best corresponds to the blue line shown in Figure 1. Then we define three new AMIP experiments, each based on this control, that are used to distinguish between the age-of-air changes resulting from changes in radiation versus changes in the handling of the REMAP algorithm (Section 3.2.1).

Specifically, these include experiments in which we a) revert back from RRTMG to the radiation from Chou and Suarez (1994) (CSRAD; Table 2, row 2), b) revert back to the MERRA-2 REMAP approach (i.e. REMAP Option 1) (M2REMAP; Table 2, row 3) and c) combine these two changes (CSRAD+M2REMAP; Table 2, row 4).

As we show in Section 3.2.1, the M2REMAP experiment produces the largest changes in age-of-air, compared to the experiment in which only the radiation is altered. To this end, we focus the remainder of our investigation (Section 3.2.2) on examining a clean set of EMIP experiments run at both C180 and C360 horizontal resolutions that distinguish the impact of REMAP Option 1 versus Option 2 on simulated transport. In particular, we perform three sensitivity experiments that differ from each other only in terms of the calculation of TE at the mid-layer pressure levels, which we perform using a linear (LINEAR; Table 2, row 5), quadratic (QUADRATIC; Table 2, row 6) and cubic interpolation (CUBIC; Table 2, row 7) scheme, with the latter corresponding to the approach that was used in MERRA-2.

These three numerical schemes are derived from the generic interpolation equation:

$$\mathcal{Q}(\mathcal{P}) = \sum_{k'} a_{k+k'} \mathcal{Q}_{k+k'} \qquad k' = 0, \pm 1, \pm 2, \ldots \qquad (1)$$

Table 2. **GEOS Model Experiments**: Targeted GEOS model experiments based off a control experiment (row 1) were carried out to identify the influence of radiation (row 2) and the FV remapping algorithm changes since MERRA-2 (row 3), as well as their combined influence (row 4). Sensitivities within the FV remapping algorithm were further explored with respect to the order of the interpolation scheme used to calculate TE at output mid-layer pressure levels (rows 5-7). Experiments in rows 1-4 are 30-year-long AMIPs run at C180 resolution, whereas rows 5-7 refer to 30-member 3-month-long (DJF) EMIP experiments. Both AMIPs and EMIPs are used for climate statistic evaluation (see Appendix A for more on the correspondence between the two). EMIP experiments are run at both C180 and C360 horizontal resolutions.

Experiment Name	Configuration	Experiment Type	Hor. Resolution
CTRL	Control, REMAP Option 2	AMIP (30 yrs.)	C180
CSRAD	Chou-Suarez (1994) Radiation (RAD)	AMIP (30 yrs.)	C180
M2REMAP	MERRA-2 REMAP Option 1 (cubic)	AMIP (30 yrs.)	C180
CSRAD+M2REMAP	Chou-Suarez (1994) RAD REMAP Option 1 (cubic)	AMIP (30 yrs.)	C180
LINEAR	MERRA-2 REMAP Option 1 (linear)	EMIP (30 mem.)	C180, C360
QUADRATIC	MERRA-2 REMAP Option 1 (quadratic)	EMIP (30 mem)	C180, C360
CUBIC	MERRA-2 REMAP Option 1 (cubic)	EMIP (30 mem)	C180, C360

where $\mathcal{P}$ represents the target output location in $\ln(p)$ and $\mathcal{Q}_{k+k'}$ denotes the surrounding grid-point values at input locations. The coefficients $a_{k+k'}$ are derived through Taylor Series expansions using non-uniform grid spacing given by:

$$a_{k+k'} = \frac{\Pi_m \left(\mathcal{P}_{k+m} - \mathcal{P}\right)}{\Pi_m \left(\mathcal{P}_{k+m} - \mathcal{P}_{k+k'}\right)} \qquad m = 0, \pm 1, \pm 2, \ldots \quad m \neq k' \qquad (2)$$

For the three schemes, the grid points used are: LINEAR $(k, k-1)$, QUADRATIC $(k+1, k, k-1)$, and CUBIC $(k+1, k, k-1, k-2)$. In all cases, the grid points are chosen such that the target location resides between layers k and $k-1$.

Note that, while the LINEAR and QUADRATIC experiments do not actually correspond to any of the model versions shown in Figure 1, they highlight the large sensitivity of the mean age to changes in the interpolation scheme that may otherwise seem innocuous. They also provide further evidence of the strong influence of changes in tropical lower stratospheric upwelling strength on the stratospheric mean age in GEOS.

Finally, in all experiments using REMAP Option 1 (i.e. M2REMAP, CSRAD+ M2REMAP, LINEAR, QUADRATIC, CUBIC) additional modifications to the divergence damping coefficients were used so as to best ensure consistency with what was used in MERRA-2. Specifically, these include changes to the number of layers for vertical sub-grid mixing, the coefficient for barotropic mode damping, the use of 2nd vs. 6th order divergence damping and the strength of the divergence damping coefficients.

2.3 Analysis Approach

2.3.1 Transport Diagnostics

To diagnose the transport circulation we focus primarily on the age-of-air (Hall and Plumb (1994)). This is inferred from an idealized global "clock" or ideal age tracer (Γ) (Thiele and Sarmiento (1990)) that is defined with respect to the bottom model level as follows: initially, the ideal age tracer is set to zero throughout the troposphere and thereafter held to zero over the entire Earth's surface, subject to a constant aging of 1 year/year throughout the atmosphere. We present here the statistically stationary (equilibrated) value of $\Gamma(r)$, which is equal to the average time since the air at a location r in the stratosphere last contacted the Earth's surface. In addition to the mean age, we also show results from an idealized e90 tracer that is uniformly emitted over the entire surface layer and decays exponentially at a rate of 90 days^{-1} such that concentrations greater than 125 ppb and less than 50 ppb tend to reside in the lower troposphere and stratosphere, respectively (Prather et al. (2011)). As this tracer features strong near-tropopause gradients and takes significantly less time to equilibrate, compared to the mean age, it is useful for evaluating stratosphere-troposphere-exchange and transport within the upper troposphere/lower stratosphere (Abalos et al. (2017, 2020); Orbe et al. (2020)).

Both the mean age and e90 tracers were integrated in all of the AMIP experiments shown in Figure 1 and listed in Table 2 (rows 1-4), which were run using the same idealized passive tracer package described in Orbe et al. (2017). Note that the mean age tracer was not integrated in the EMIP experiments given its much longer characteristic timescale in the stratosphere ($\sim$ 3-5 years). As such, the EMIP simulations, which do not exceed one year, are not appropriate for evaluating the time-integrated transport characteristics reflected in the age-of-air.

In addition to carrying the idealized tracers, two of the experiments shown in Figure 1 were also run with full interactive chemistry and correspond to the two CCMI (Phase 1 and Phase 2) integrations (red and green lines, Figure 1). Both simulations employ the same Global Modeling Initiative (GMI) chemical mechanism (Strahan et al. (2013)) and are therefore useful in evaluating the impact of age differences on real trace gas distri-

butions. In particular, as shown in Section 3.1 results from these experiments show significant imprints of the age-of-air changes on nitrous oxide (N_2O) and methane (CH_4).

2.3.2 Circulation Diagnostics

As we show in Section 3, the changes in age-of-air across the different model versions are strongly tethered to changes in the advective component of the circulation, which we quantify using the Transformed Eulerian Mean (TEM) estimate of the Lagrangian transport of mass by the circulation. Thus, in addition to more standard Eulerian metrics of the circulation (e.g., zonal winds and temperatures), we focus on the vertical component of the TEM residual velocity, defined as $\overline{w}^* = \overline{w} + \frac{\partial(\psi cos\phi)}{acos\phi\partial\phi}$, where $\psi = \overline{v'\theta'}/\frac{\partial\overline{\theta}}{\partial p}$ is the eddy stream function, θ refers to potential temperature, a is the Earth's radius and overbars and primes denote zonal means and deviations therefrom, respectively (Andrews et al. (1987)). In addition, we interpret the behavior in w^* using the Eliassen-Palm flux divergence ($\nabla \cdot F$), whose horizontal ($F(\phi)$)and vertical ($F(p)$) components are respectively defined as $F(\phi) = acos\phi[\frac{\partial u}{\partial p}\psi - \overline{u'v'}]$ and $F(p) = acos\phi([f - \frac{\partial \overline{ucos\phi}}{acos\phi\partial\phi}]\psi - \overline{u'\omega'})$.

2.4 Observations and Reanalyses

While our focus is on interpreting and understanding the different model configurations, we incorporate observations to provide context when possible, although we do not present an exhaustive evaluation of the model's transport characteristics (for that see earlier studies including Orbe et al. (2017, 2018)). However, as the tracers are not directly integrated in MERRA-2 (with the exception of ozone), we compare against independent observational estimates. For the mean age we first compare simulated meridional age profiles at 50 hPa with values derived from in situ aircraft measurements of carbon dioxide (CO_2), averaged in 2.5 degree latitude bins over the altitude range 19.5 to 21.5 km (Boering et al. (1996), see also Figure 5 in Hall et al. (1999)).

We also briefly evaluate impacts of transport biases on the simulated trace gas distributions for the CCMI Phase 1 and 2 experiments. The simulated fields of methane (CH_4) are compared with the climatologies derived for 1991–2002 from the Halogen Occultation Experiment (HALOE) on board the Upper Atmosphere Research Satellite (UARS) (Grooß and Russell III (2005)). Comparisons of simulated nitrous oxide (N_2O) are made against climatologies derived from the Microwave Limb Sounder (MLS) on the Earth Observing System (EOS) Aura satellite. Climatologies over the same period (2005–2015) are used to evaluate both the model and the observations. We use the 190-GHz retrieval from Version 4.2 because the 640-GHz data set ends in summer 2013 due to the failure of the N_2O primary band.

For the circulation diagnostics nearly all comparisons are made relative to the MERRA-2 data assimilation (DAS) reanalysis product, noting that comparisons against ERA-5 (not shown) reveal a similar picture. One exception, however, is the vertical component of the TEM circulation (w^*), which shows some differences in vertical structure between MERRA-2 and a 30-member ensemble of (free-running) AMIP integrations produced using the MERRA-2 model, hereafter referred to as M2AMIP (Collow et al., 2017)(Appendix Figure A1, right). As the free-running model results shown in Figure 1 show more consistency with the vertical profile of M2AMIP, not MERRA-2, we compare w^* in all free-runnning GEOS experiments with M2AMIP, noting that for non-derived measures (i.e., winds, temperatures), the raw MERRA-2 output is used.

The differences in w^* between M2AMIP and MERRA-2 may reflect the influence of temperature increments in the DAS (MERRA-2) which can drive spurious vertical transport in assimilated products (Weaver et al., 1993; Orbe et al., 2017). In particular, Weaver et al. (1993) showed that the imbalance between the thermal and velocity fields at the time an observation is ingested during the assimilation cycle can excite unwanted inertial-
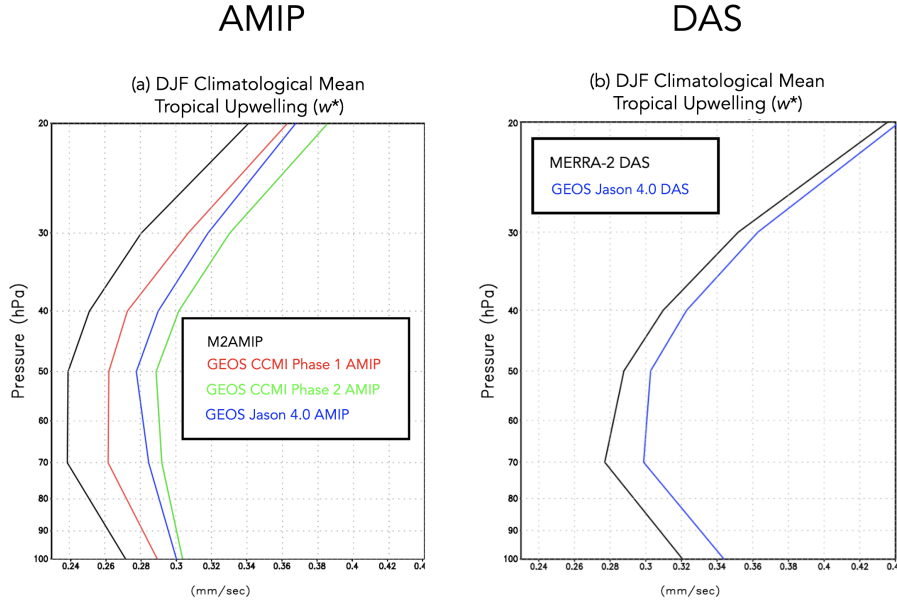
Figure 2. Left: The DJF climatological mean vertical residual mean velocity, w^*, averaged between the turnaround latitudes for GEOS free-running AMIP simulations using the model configurations corresponding to the CCMI Phase 1 (red) and Phase 2 (green) submissions and to Jason 4.0 (blue). M2AMIP is shown in black. Right: The DJF climatological mean vertical residual mean velocity, w^*, averaged between the turnaround latitudes for MERRA-2 (black) and a data-assimilation configuration of Jason 4.0 (blue). Note that the right panel only uses limited data from years 1997-2021 for which the Jason 4.0 DAS output was available. As they reflect more recent years, the MERRA-2 DAS values in the right panel are therefore larger than the values shown in Figure A1b, given that w^* has increased over more recent decades (see Figure 5.14 in (Fujiwara et al., 2022)).

gravity wave modes that manifest strongly in the residual vertical winds. This impact of the increments may therefore explain the differences in w^*, particularly above 30 hPa, where the contribution of temperature increments to the analysis is large. We emphasize, however, that our main interest in this study is on upwelling within the lower stratosphere (i.e., 70-100 hPa), where M2AMIP and MERRA-2 agree well, as this region best correlates with the global age-of-air characteristics. As such, we reserve further exploration of the w^* differences above 50 hPa for future work.

3 Results

3.1 Reduction of Stratospheric Mean Age in GEOS Models Since MERRA-2

We begin by interpreting the reduction in mean age exhibited in more recent model versions in terms of changes in the strength of upwelling in the tropical lower stratosphere. In particular, the reductions in Γ (Figure 1) are consistent with increases in the strength of lower stratospheric tropical upwelling, with w^* becoming progressively stronger in more recent model tags, relative to MERRA-2 (Figure 2a). Note that, while the increases in w^* occur throughout the stratosphere, we focus on the changes occurring between 70 and 100 hPa as these are most relevant to determining the tropical upward mass flux and associated strength of the mean overturning circulation.

Interestingly, the increases in w^* relative to MERRA-2 are not only manifest in 30-year-long AMIPs (Fig. 2a), but also in a DAS configuration of the Jason 4.0 model tag (Fig. 2b), evaluated over a more recent period spanning 1997 to 2021. Though not the main focus of this study, this impact on the DAS simulations has important implications for the development of R21C as it highlights that the assimilation of observations may reduce, but not entirely correct for, the model transport biases that have been introduced in more recent GEOS model versions.

Though perhaps naive, the relationship between lower stratospheric upwelling and the mean age suggested by comparing Figure 1 and Figure 2a is consistent with the long-term behavior of Γ inferred from both historical and projected future climate simulations (Butchart et al. (2010); Abalos et al. (2021)). A strong relationship between the strength of lower stratospheric ascent and the mean age was also shown to hold in the CCMVal models (see Fig. 5.20 in J. Neu et al. (2010)). Nevertheless, it is important to note that a clear relationship between w^* and Γ is not a priori expected, as the age-of-air is also known to be very sensitive to mixing, which may be important in interpreting differences among the CCMI Phase 1 models (Dietmüller et al. (2018)).

The differences in w^* highlighted in Figure 2 are associated with enhanced Eliassen-Palm flux convergence over NH midlatitudes (Figure 3). Increased wave convergence is evident not only within the subtropical lower stratosphere ($< 30°$N, 50-100 hPa) but also over higher latitudes and altitudes ($\sim 40°$-$70°$N, 20-50 hPa). The fact that differences in extratropical wave convergence imprint on tropical upwelling is consistent with our understanding of the so-called "downward control" principle (Haynes et al. (1991)).

In particular, the strength of the residual mean streamfunction (Ψ^*) is, via downward control, directly related to the vertically integrated eddy-induced total zonal force above that level and has contributions both from the (resolved wave) Eliassen-Palm flux divergence (Figure 3) as well as the gravity wave drag scheme's parameterized waves (not shown). The tropical upward mass flux – defined as Ψ^*_{max}-Ψ^*_{min} evaluated at the turnaround latitudes (e.g. Rosenlof (1995)) – is therefore directly dependent on the wave forcing aloft.

One subtlety to note is that the wave convergence changes shown in Figure 3 occur at high latitudes and are directly associated with downwelling over the polar region. It is then via mass balance that anomalously strong downwelling associated with enhanced

DJF Climatological Mean Eliassen-Palm Flux Divergence ($\nabla \cdot \mathbf{F}$)
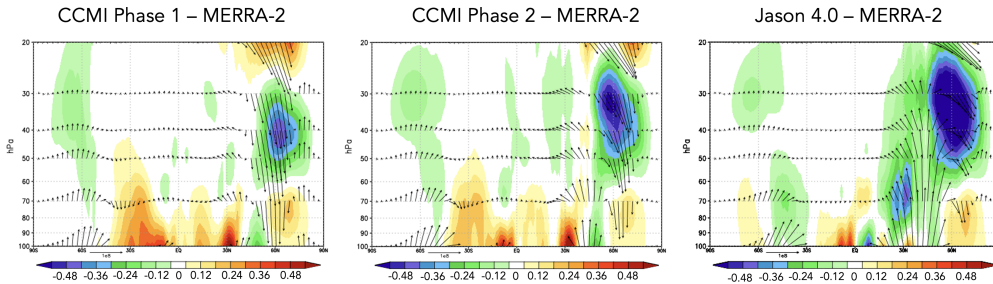

Figure 3. Colors show anomalies in the DJF climatological mean Eliassen-Palm (EP) flux divergence between the CCMI Phase 1 (left), CCMI Phase 2 (middle) and Jason 4.0 GEOS AMIP (right) model versions, relative to MERRA-2. Arrows denote anomalies in the vertical and meridional EP flux vectors (relative to MERRA-2).

flux convergences must be accompanied by enhanced upwelling in the tropics. This indirect impact of higher latitude wave drag reflects an "extratropical pumping" mechanism (Holton et al., 1995), which is illustrated more clearly in Section 3.2.2 in the context of the LINEAR, QUADRATIC and CUBIC experiments.

While the reduction in Γ (Figure 1) of $\sim 30\%$ at 50 hPa is significant, it is neither clear if this change is representative of other altitudes within the stratosphere nor how this age bias imprints on real chemical species. To this end, we begin by comparing the full latitude-pressure distribution of changes in Γ and another passive tracer (e90) (Figure 4) between the CCMI Phase 1 and Phase 2 model configurations (red and green lines, Figure 1). In particular, we find that the changes in both passive tracers – large reductions in Γ within both hemispheres (Fig. 4, top right) and increased values of e90 within the lower stratosphere (Fig. 4, bottom right) – are reflective of an overall increase in the strength of the transport circulation. This is highlighted in the CCMI Phase 2 – 1 model differences for the passive tracer distributions (Fig. 4, right panels) which are shown in the absence of robust observational constraints of Γ at higher altitudes (or any observational constraints for e90, for that matter). The reduced/increased stratospheric burdens of the age and e90 tracers are consistent with stronger upwelling in the CCMI Phase 2 model configuration (Figure 2).

While the observational constraints on Γ presented in Figure 1 and the departure of w^* away from MERRA-2 suggest that transport properties of the newer model configurations are moving in the wrong direction, it is relevant to ask whether or not the trace gas satellite measurements also support this conclusion. Indeed, comparisons with observations show larger biases in N_2O (Fig. 5, top panels) and CH_4 (Fig. 5, bottom panels), increasing from 10% to 30% in the CCMI Phase 2 model configuration, depending on the species. The patterns of these biases are generally consistent with the biases in the mean age (Fig. 4), suggesting a strong link between the tracers. Recall that the same chemistry mechanism is used in both CCMI Phase 1 and 2 simulations.

The fact that the mean age changes have a significant imprint on the simulated trace gases is consequential for the GEOS-R21C system. However, the configurations shown in Fig. 1-5 differ in many respects (physics, resolution, radiation, FV remapping algorithm) and it is difficult to meaningfully interpret what is driving the changes in w^* (and the tracers). We therefore move next to the targeted model experiments (Table 2) in or-
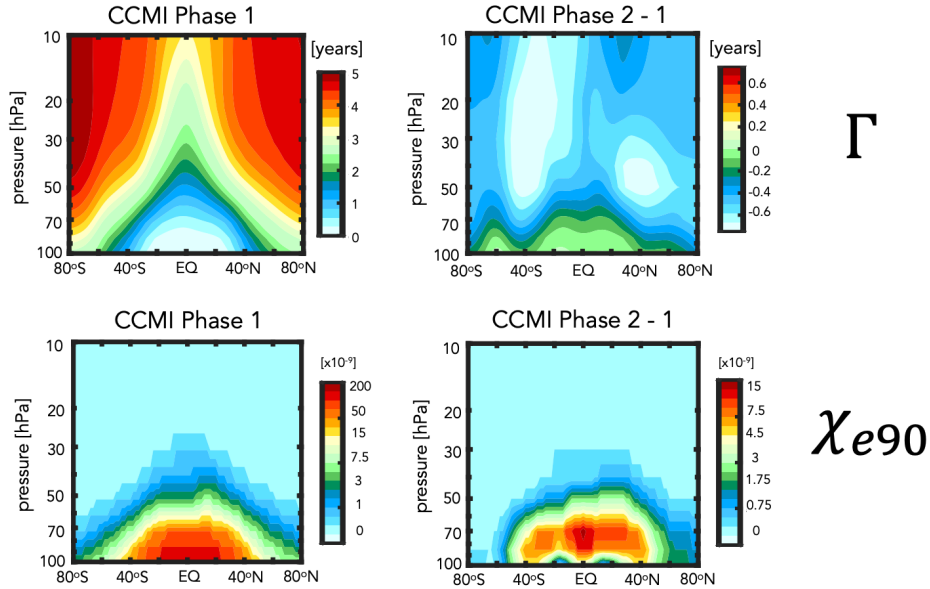
Figure 4. The climatological mean (2000-2010) distribution of the mean age-of-air (Γ) (left, top) and e90 idealized tracers (left, bottom) for the CCMI Phase 1 model configuration. Climatological differences between the CCMI Phase 2 and Phase 1 model configurations are shown in the right panels. Note that a nonlinear colorbar has been used in the e90 subplots.

der to interpret the model development steps that resulted in these transport circulation changes.

3.2 Identifying Drivers of Upwelling and Tracer Changes Since MERRA-2

3.2.1 *Radiation versus REMAP Algorithm*

As discussed in Section 2, among the model changes that were made since MERRA-2, the changes in radiation and the FV remapping algorithm are most likely to directly have impacted the stratospheric circulation. We therefore begin by assessing which of these changes dominates the decreases in Γ shown in Figure 1.

Figure 6 shows the distribution of Γ for experiments in which the longwave, shortwave, and REMAP updates since MERRA-2 have successively been undone. Relative to the control experiment (CTRL; Table 2, row 1), the reversion back to Chou and Suarez (1994) in the shortwave and Chou (1990, 1992) in the longwave results in an increase in the mean age of ~ 0.5 years throughout the stratosphere (CSRAD; Table 2, row 2). Though significant, this change in Γ is smaller than the change that results from reverting back to REMAP Option 1 (M2REMAP; Table 1; row 3), in which the mean age increases by ~ 1 year. The combined impacts of both changes (CSRAD+M2REMAP; Table 1 row 4) is roughly linear, with age values of ~ 5.5 years over high latitudes at 50 hPa, consistent with the values simulated by the GEOS-CTM MERRA-2 integration (black line, Figure 1) and with the CCMI Phase-1 version of the model (red line, Figure 1).

Next we ask if the behavior of Γ exhibited in Figure 6 can be interpreted in terms of changes in the strength of lower stratospheric tropical upwelling and extratropical wave
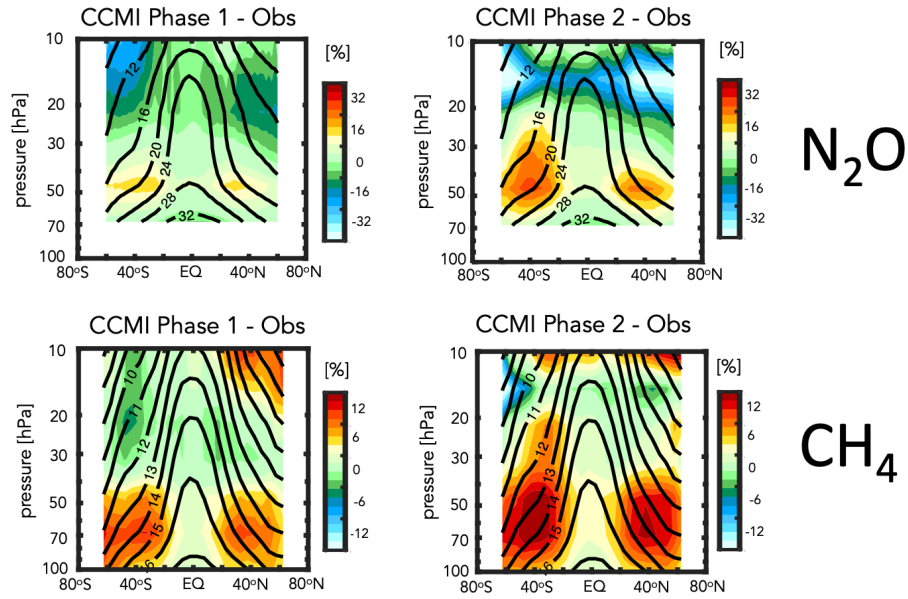
Figure 5. Colors shown anomalies in the simulated distributions of nitrous oxide (N_2O) (top) and methane (CH_4) (bottom), relative to the MLS and HALOE observed values, respectively, for the CCMI Phase 1 (left) and Phase 2 (right) GEOS model configurations. Climatological mean observed values are shown in the black contours.
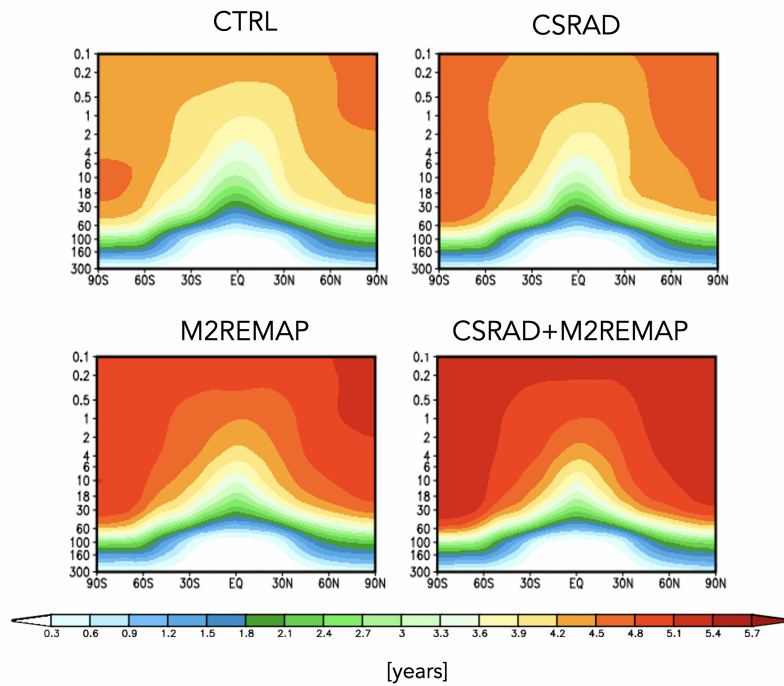
Figure 6. Colors show the simulated 2000-2010 climatological annual mean distributions of the mean age-of-air (Γ) for the CTRL (top left; Table 1, row 1), CSRAD (top right; Table 1, row 2), M2REMAP (bottom left; Table 1, row 3) and combined CSRAD+M2REMAP (bottom right; Table 1, row 4) experiments.

DJF Climatological Mean Tropical Upwelling (w^*)
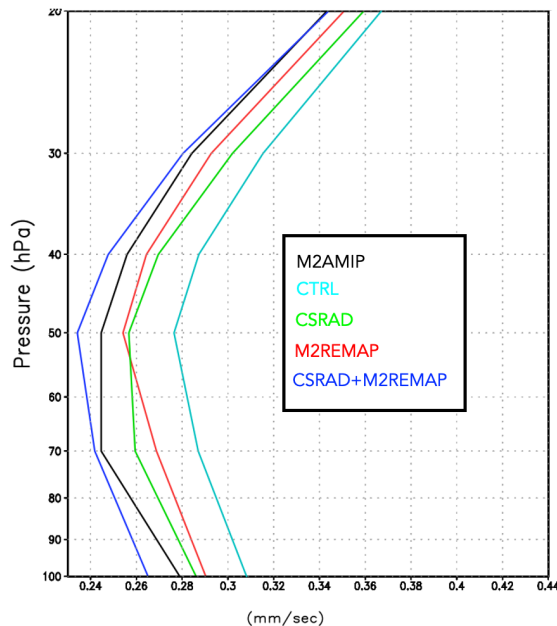
Figure 7. The DJF 1985-2015 climatological mean vertical residual mean velocity, w^*, averaged between the turnaround latitudes for the CTRL (cyan line; Table 2, row 1), CSRAD (green line; Table 2, row 2), M2REMAP (red line; Table 2, row 3) and combined CSRAD+M2REMAP (blue line; Table 2, row 4) experiments. M2AMIP is shown in black.

convergence, as our previous analysis of the CCMI experiments suggested. Indeed, Figure 7 shows that values of upwelling decrease in the CSRAD and M2REMAP experiments, relative to the CTRL integration. The increase in upwelling resulting from both changes (CSRAD+M2REMAP) is still larger, consistent with the larger age decreases in that experiment. This change in the behavior of w^* within the tropical stratosphere can be interpreted in terms of changes in the Eliassen Palm flux convergence over NH midlatitudes (not shown), which features smaller values in the CSRAD, M2REMAP (and CSRAD+ MSREMAP) experiments. Note that our examination of the changes in w^* are derived from EMIP integrations, which we showed previously converge (for DJF) to the statistics derived from corresponding AMIP experiments.

3.2.2 FV REMAP Algorithm: Sensitivity of Climate Statistics

Having shown in the previous section that the largest changes in the mean age were realized through the reversion back to REMAP Option 1, we now investigate further the sensitivity of the transport circulation to the choice of remapping interpolation scheme. In particular, we compare simulations in which total energy is calculated at new midlayer pressures using cubic, quadratic and linear interpolation prior to the aposterior integral conservation (Table 2, rows 5-7). In addition, in this section we seek to understand how the changes in the Eliassen-Palm flux convergence over NH midlatitudes arise via analysis of the large-scale wind structure.

Figure 8 (left panel) shows a clear sensitivity in tropical upwelling to the choice of interpolation scheme, with w^* progressively increasing in strength moving from the CUBIC to QUADRATIC to LINEAR schemes. This sensitivity is robust across horizontal

DJF Climatological Mean Upwelling ($w*$)
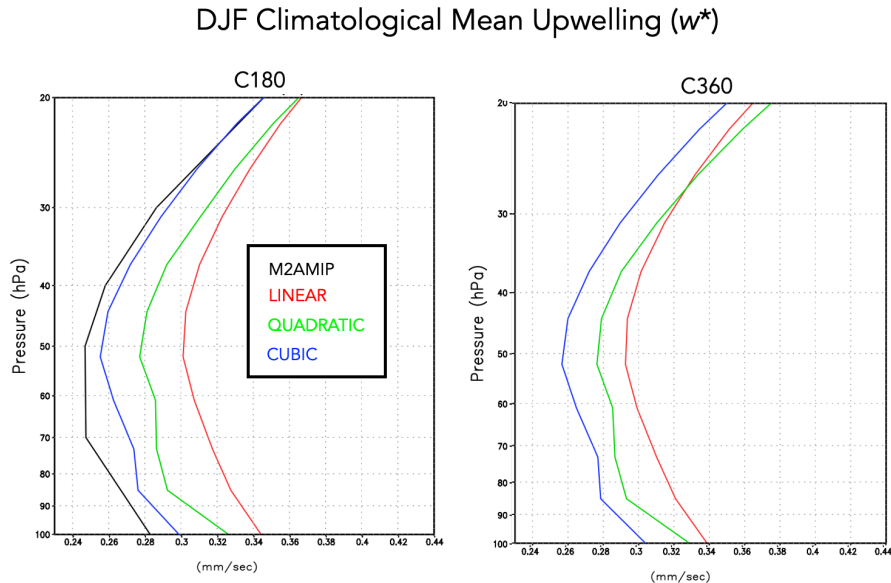
Figure 8. The DJF 1985-2015 climatological mean vertical residual mean velocity, w^*, averaged between the turnaround latitudes for the LINEAR (red line; Table 2, row 5), QUADRATIC (green line; Table 2, row 6) and CUBIC (blue line; Table 2, row 7) experiments. M2AMIP is shown in black. Results from C180 and C360 EMIP experiments are shown in the left and right panels, respectively.

resolutions as the same suite of experiments performed at C360 exhibit the same sensitivity (Fig. 8, right panel). While no current model version actually employs a linear scheme, this suite of experiments highlights the strong sensitivity to choice of interpolation scheme within the remapping algorithm; to the best of our knowledge, this result has not been reported in the literature. Furthermore, as we show next, this clean set of experiments allow us to inquire mechanistically into the processes that are driving the changes in wave convergence over midlatitudes, unencumbered by differences in horizontal resolution, physics, etc.

Consistent with our expectations based on the analysis of the previous experiments, the drivers of the changes in w^* are related to increased wave convergence moving from the CUBIC to QUADRATIC to LINEAR schemes (Figure 9). Over extratropical latitudes, the zonal force associated with this enhanced wave convergence is associated with enhanced downwelling at high latitudes that, through mass balance, is accompanied by enhanced upwelling in the tropics. This indirect impact of higher latitude wave drag is evident in Appendix Figure C1, which shows stronger upwelling/downwelling in the LINEAR and QUADRATIC experiments over the tropics/polar region.

Next we exploit the fact that these experiments only differ with respect to the interpolation scheme in order to inquire further into the drivers of the wave convergence changes. To this end, Figure 10 compares profiles of the zonal mean zonal wind between the CUBIC, QUADRATIC and LINEAR experiments, averaged over the region of enhanced wave convergence (i.e. 20°N-60°N). The experiments featuring stronger wave convergence (LINEAR and QUADRATIC) are also simulations with stronger zonal winds, relative to MERRA-2, especially above 70 hPa. This change in winds occurs at both C180 (Fig. 10, left panel) and C360 (Fig. 10, right panel) resolutions.

DJF Climatological Mean Eliassen-Palm Flux Divergence ($\nabla \cdot F$)
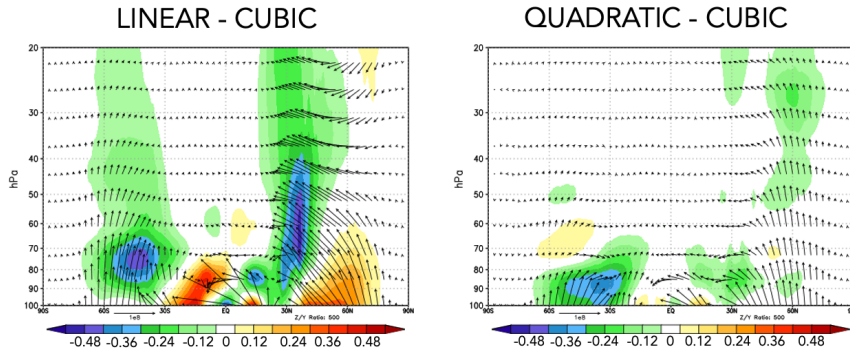
Figure 9. Colors shown anomalies in the DJF 1985-2015 climatological mean Eliassen-Palm (EP) flux divergence in the LINEAR (left) and QUADRATIC (right) experiments, relative to the CUBIC model experiment. Arrows denote anomalies in the vertical and meridional EP flux vectors.

Structurally, the increase in zonal wind strength over northern extratropical mid-latitudes is reflective of a poleward shift in the zonal winds as the critical latitude, i.e. where the zonal wind is zero, shifts northward in the QUADRATIC and, especially, LIN-EAR integrations, relative to the CUBIC experiment (Figure 11). Since stationary waves only propagate in westerly zonal flow, the latitude where zonal flow is zero acts a bound-ary for wave propagation (Hardiman et al. (2014)). As a result, this shift in critical lat-itude results in enhanced wave propagation and convergence over middle and high lat-itudes.

Figures 10 and 11 highlight how the changes in zonal winds in the LINEAR and QUADRATIC experiments reflect a degradation in model skill, relative to MERRA-2, throughout the entire stratosphere. The changes in upwelling, mean age, chemical trace gases and zonal winds thus provide a coherent and self-consistent picture suggestive of a degradation in the representation of the stratospheric circulation since MERRA-2. That is, an increased bias in the stratospheric northern zonal winds are, via their influence on wave convergence, compromising changes in the strength of the mean meridional over-turning circulation and its impact on composition. It is interesting to note that the wind biases also extend into the troposphere and show degraded skill relative to MERRA-2 in the LINEAR and QUADRATIC experiments (Figure 11). Examination of other fields (i.e. tropopause biases, Appendix Figure D1) present somewhat more of a nuanced story that depends more sensitively on latitude and season considered. The improvements in the zonal winds, however, are most relevant for setting the upwelling characteristics within the tropical lower stratosphere via their influence on wave propagation into that region.

Finally, to better understand why these impacts on the winds have such a conse-quence for the wave convergence properties within the stratosphere, next we examine the zonal structure of these biases in the middle stratosphere (Figure 12). This reveals that the enhanced winds in the LINEAR (and, to a lesser extent, QUADRATIC) integrations are concentrated over the North Pacific at both C180 (Fig. 12, left) and C360 (Fig. 12, right) resolutions (a similar picture emerges within the troposphere, not shown). As this region is the primary region dominating the stationary component of the upward flux of vertical wave activity (Plumb (1985), see their Figure 4) it is perhaps not surprising

DJF Climatological Mean Zonal Wind (20ºN-60ºN)
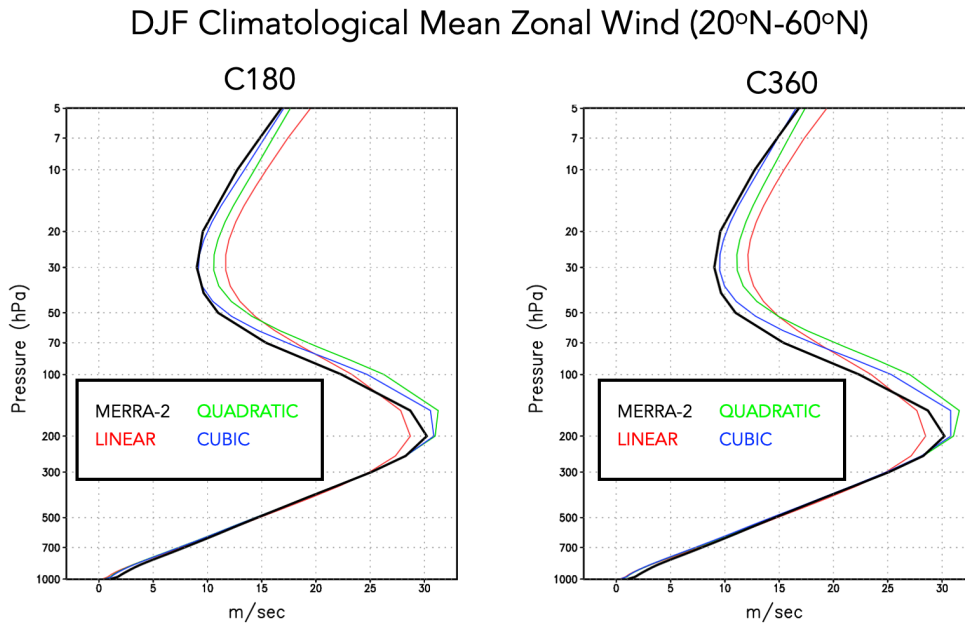
Figure 10. Vertical profiles of the DJF 1985-2015 climatological mean zonal mean zonal winds in the LINEAR (red), QUADRATIC (green) and CUBIC (blue) experiments, averaged between 20°N and 60°N. MERRA-2 is shown in the black line. Results for both C180 (left) and C360 (right) experiments are shown.

that this region is having a profound impact on the mean overturning circulation. Again, as with the zonal mean wind changes, the increases in wind strength over the North Pacific represent degraded model skill relative to MERRA-2. Note that comparisons with ERA-5 reveal a similar bias (not shown).

4 Conclusions

Here we have performed an analysis aimed at understanding differences in the representation of the stratospheric circulation in recent candidate systems for GEOS-R21C, relative to older versions of GEOS similar to the model used to produce MERRA-2. Using targeted experiments oriented at disentangling various model development updates, we have identified a key role played by changes in the remapping algorithm within the model's finite-volume dynamical core. Our key results are as follows:

#1. The stratospheric mean age-of-air in GEOS is sensitive to the degree of the interpolation scheme that is used to calculate layer-mean values of total energy, U, V and tracers. Different treatment of the vertical remapping algorithm (REMAP Option 1 vs. 2) result in mid-stratospheric (50 hPa) age-of-air differences of ~ 1 year over high latitudes, or about 30% climatological mean values.

#2. The age-of-air sensitivities reflect, to first order, changes in the strength of tropical upwelling associated with the Brewer-Dobson circulation which are in turn are driven by changes in EP flux convergence over northern midlatitudes. Changes in wave convergence reflect shifts in (critical lines of) wave propagation that originate in the troposphere over the Pacific Ocean, a region of strong upward wave activity.

DJF Climatological Zonal Mean Zonal Wind Anomalies Relative to MERRA-2
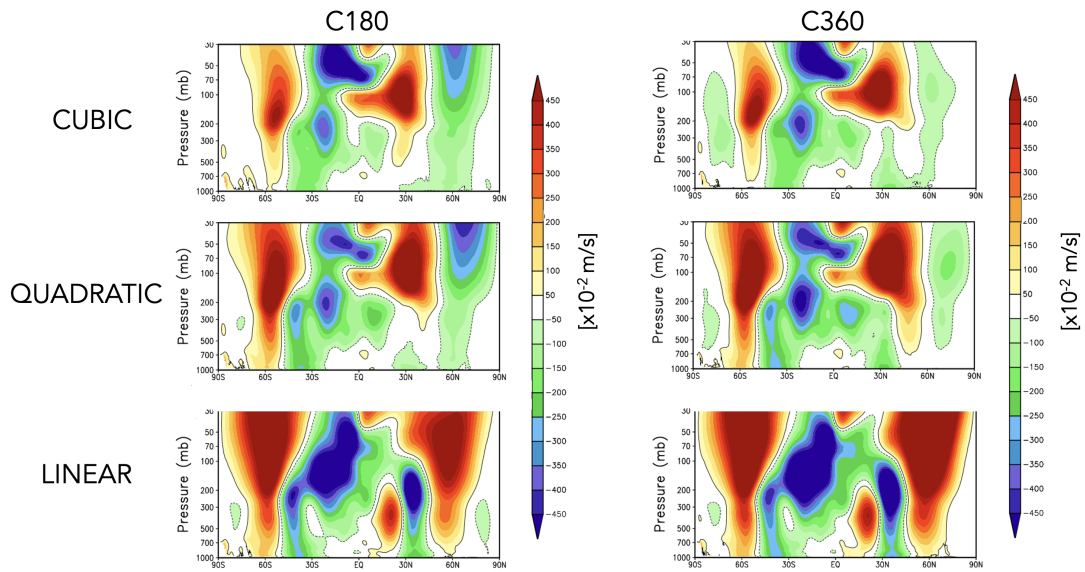
Figure 11. Colors shown anomalies in the DJF 1985-2015 climatological mean zonal mean zonal winds in the CUBIC (top), QUADRATIC (middle) and LINEAR (bottom) experiments, relative to MERRA-2. Results for both C180 (left) and C360 (right) experiments are shown.

DJF Climatological 30 hPa Zonal Wind Anomalies Relative to MERRA-2
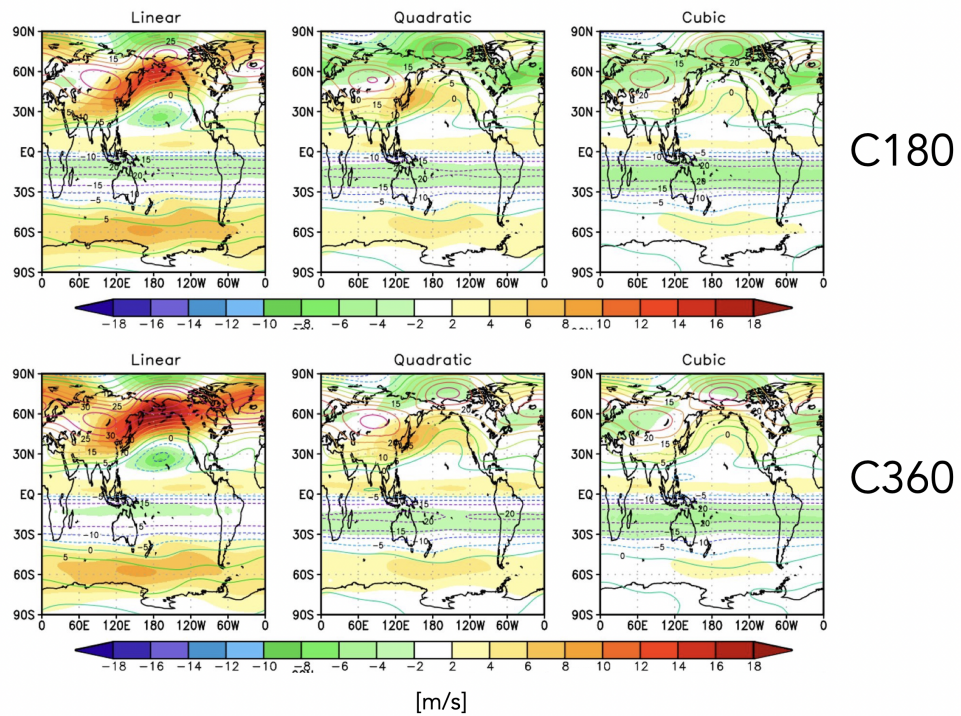
Figure 12. Colors shown anomalies in the DJF 1985-2015 climatological mean zonal winds at 30 hPa in the CUBIC (right), QUADRATIC (middle) and LINEAR (left) experiments, relative to MERRA-2. Results for both C180 (top) and C360 (bottom) experiments are shown.

#3. The degradation of upwelling statistics manifest in AMIPs, also translate to degradations in DAS configurations of GEOS.

Although our focus here has been on the stratospheric transport circulation, motivating our use of tracer-independent metrics like the age-of-air, our results have clear implications for constituent transport in the next reanalysis that is currently under development (GEOS-R21C). In particular, we showed that the increased age-of-air biases correspond to increased biases in the representations of CH_4 and N_2O moving from the CCMI Phase 1 to Phase 2 model configuration. This comports with well-known correlations between the mean age and stratospheric trace gases, reinforcing the fact that model transport inaccuracies continue to significantly affect simulations of important long-lived chemical species in the stratosphere (Hall et al. (1999)).

Our results highlight the key role played by model numerics in transport (e.g., Rood (1987)). The sensitivities in the age-of-air documented herein are also consistent in spirit with the findings in Gupta et al. (2020) who showed significant age differences occurring between spectral versus finite-volume numerics. Our results, however, suggest that there remain large sensitivities even within a given (FV) dynamical core. Furthermore, we also briefly show that that statistics derived from long AMIPS also manifest within a data assimilation context, which raises important questions as to the degree to which model biases can be ameliorated through assimilation of observations.

Looking forward, our findings support and build on the recommendation proposed in Gupta et al. (2020) for the construction of dynamical core benchmark tests aimed at determining how underlying AGCM numerics impact climatological transport properties. In particular, in addition to the age-of-air, the authors propose a range of stratospheric circulation diagnostics that should be evaluated including the zonal mean zonal winds, eddy temperature variance and zonal spectra of eddy kinetic energy. Our analysis reveals an important role to be played by the climatological zonal mean wind structure as it impacts wave convergence over midlatitudes; we therefore also recommend explicit consideration of the Eliassen Palm flux convergence and tropical upwelling (w^*) fields as they may be crucial for interpreting age-of-air changes.

One somewhat incidental – but practical - result from our analysis is that the statistics of $\nabla \cdot F$ and w^* are well approximated by ensembles of so-called EMIP integrations. As these are substantially easier to run than AMIPs these could provide a "first pass" when evaluating new proposed model development changes, without the immediate need to integrate AMIP-style experiments. We emphasize, however, that this statement should only apply to a first stage in model development as the age-of-air will reflect the time integrated impacts of both advection and mixing.

Finally, we conclude by noting that, while we have focused on sensitivities within the FV remapping algorithm, our results have highlighted important sensitivities to changes in radiation and, to a lesser extent, changes in parameterized convection. Though not the dominant drivers of the age-of-air changes identified here, the former could potentially influence the age both directly through changes in thermal structure and indirectly by modifying wave propagation and/or generation in the troposphere. Future work will focus on examining these impacts.
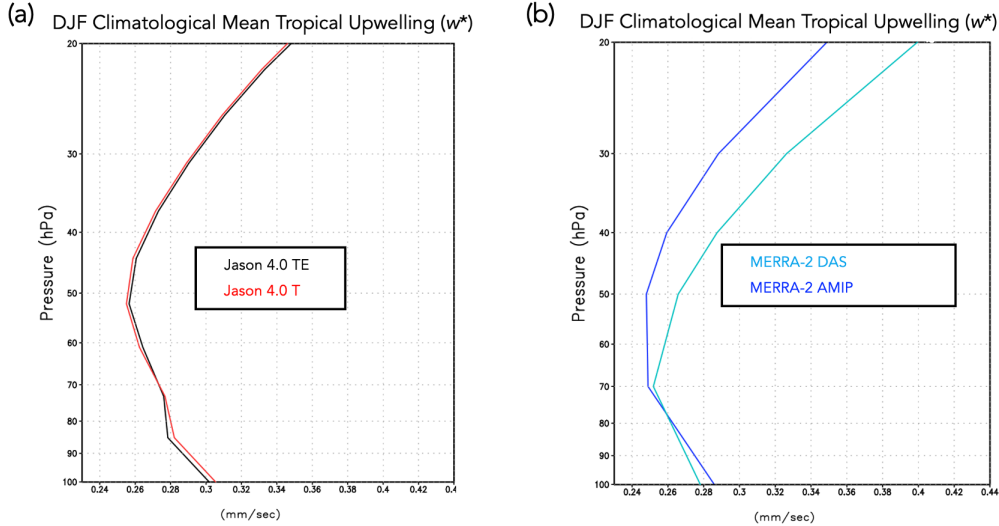
Figure A1. The DJF 1985-2015 climatological mean vertical residual mean velocity, w^*, averaged between the turnaround latitudes compared between two Jason 4.0 experiments remapping to temperature (T) (red) versus total energy (TE) (black) (a) and between MERRA-2 DAS (cyan) and the M2AMIP ensemble (blue) (b).

Appendix A Sensitivities in Calculation of TEM Upwelling

There are various aspects of the calculation of the TEM circulation that warrant further comment. First, whereas the modeling experiments listed in Table 2 (rows 5-7) focus on the sensitivity of Step 5 in REMAP Option 1 to the choice of interpolation scheme, another difference between REMAP Options 1 and 2 is the use of TE versus T, respectively. To test the impact of this difference, we ran a new experiment which is identical to the CUBIC experiment (Table 2, row 7), except that T is remapped from input layer mean pressure locations to standard output layer mean locations directly using cubic interpolation (i.e., no computation of TE or a-posteriori energy conservation applied). Appendix Figure A1a shows that this has little impact on the strength of tropical upwelling, suggesting that the w^* differences between REMAP Options 1 and 2 are dominated by sensitivities to the choice of interpolation scheme, not the use of TE versus T.

Second, the vertical component of the TEM circulation (w^*) shows some differences in vertical structure between MERRA-2 and the 30-member M2AMIP ensemble (Appendix Figure A1b). This difference in vertical structure appears to reflect a difference between DAS and free-running configurations of the model, since both DAS configurations shown in Figure 2b share a similar vertical structure. Given this difference, we ensure as apples-to-apples a comparison of simulated TEM velocities by comparing all AMIP results to other AMIPS, and vice versa for the few selected DAS results.

## Appendix B Correspondence between EMIP and AMIP Upwelling

Appendix Figure B1 shows the close correspondence in DJF climatological mean w^*, averaged between the turnaround latitudes, from AMIP and EMIP experiments using the same model configuration. This good agreement in upwelling is used to justify the analysis of the EMIP experiments listed in Table 2 (rows 5-7).
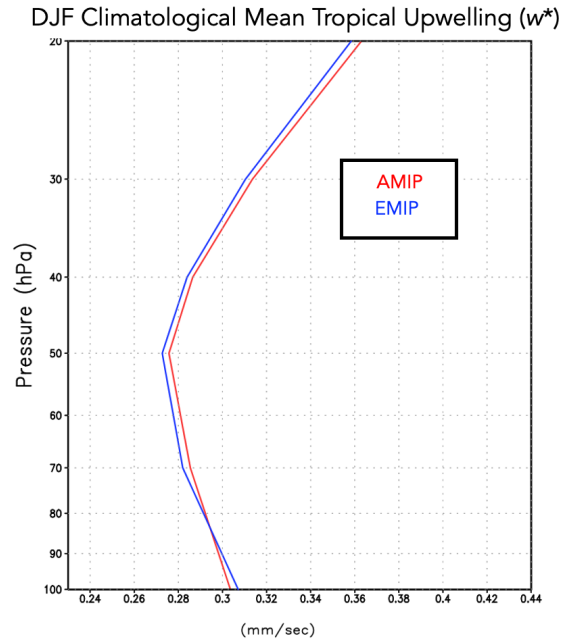
Figure B1. The DJF 1985-2015 climatological mean vertical residual mean velocity, w^*, averaged between the turnaround latitudes for the CTRL experiment (Table 2, row 1). Results based on a 30-year-long AMIP experiment (red line) and a 30-member ensemble of three-month-long EMIP experiments (blue line) are shown.

## Appendix C Changes in Tropical and High Latitude Upwelling

Appendix Figure C1 compares the behavior in residual mean upwelling among the LINEAR, QUADRATIC and CUBIC experiments over the latitudes between the (tropical) turnaround latitudes (left) and poleward of the northern turnaround latitude (right). The ordering among experiments in both regions reflects how increases in downwelling at high latitudes are, through mass balance, accompanied by enhanced upwelling in the tropics.

DJF Climatological Mean Upwelling (*w**)
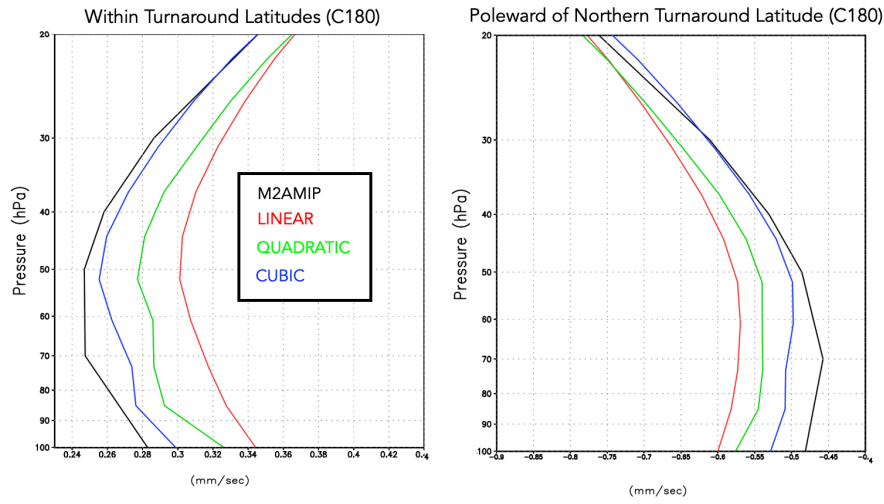
Figure C1. Left: The DJF 1985-2015 climatological mean vertical residual mean velocity, w^*, averaged between the turnaround latitudes for the LINEAR (red line; Table 2, row 5), QUADRATIC (green line; Table 2, row 6) and CUBIC (blue line; Table 2, row 7) experiments. M2AMIP is shown in black. Right: As in left panel, except averaged over latitudes poleward of the northern turnaround latitude. Results in both panels are shown for C180 experiments.

Appendix D Tropopause Pressure

Appendix Figure D1 compares boreal winter tropopause pressure and temperature among the LINEAR, QUADRATIC and CUBIC experiments, relative to MERRA-2.

DJF Climatological Mean Tropopause
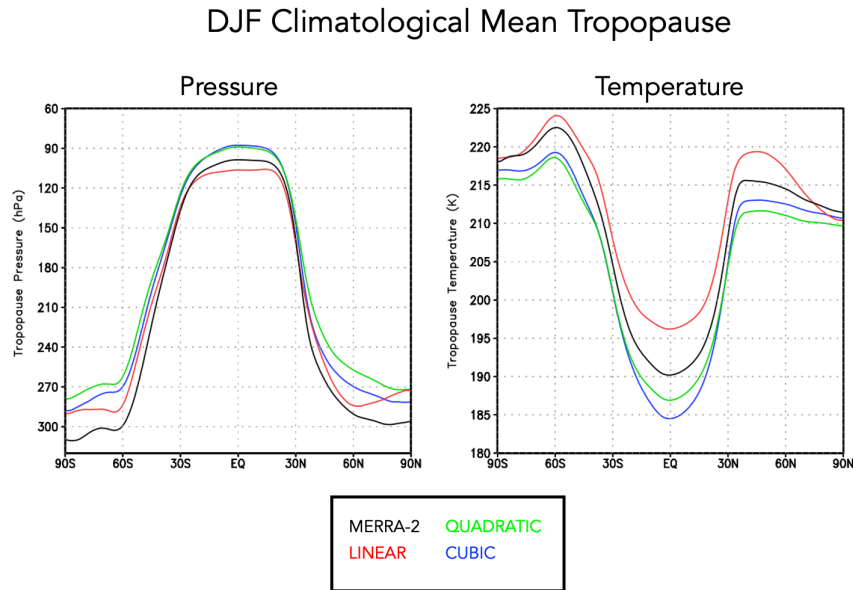
Figure D1. The DJF 1985-2015 climatological mean tropopause pressure (left) and temperature (right) in the CUBIC (blue), QUADRATIC (green) and LINEAR (red) experiments. MERRA-2 is shown in black. Results are shown for the C180 experiments.

Acronyms

AMIP Atmospheric Model Intercomparison Project

CH$_4$ methane

CCMs chemistry climate models

CCMI Chemistry Climate Modeling Initiative

CCMVal Chemistry Climate Model Validation

CO$_2$ carbon dioxide

CTRL control

CTM chemistry transport model

DAS Data assimilation

DJF December-January-February

EMIP ensemble AMIP

EOS Earth Observing System

EP Eliassen-Palm

FV finite volume

GEOS Global Earth Observing System

GEOS-R21C GEOS Retrospective analysis for the 21st Century

GMI Global Modeling Initiative

HALOE Halogen Occultation Experiment

MERRA-2 Modern-Era Retrospective Analysis for Research and Applications v2

MLS Microwave Limb Sounder

N$_2$O nitrous oxide

NH northern hemisphere

PPM piecewise parabolic

RRTMG Rapid Radiative Transfer Model for GCMS

SW shortwave

TE total energy

TEM Transformed Eulerian Mean

UARS Upper Atmosphere Research Satellite

Open Research Section

TBD

Acknowledgments

References

Abalos, M., Calvo, N., Benito-Barca, S., Garny, H., Hardiman, S. C., Lin, P., . . . others (2021). The Brewer–Dobson circulation in CMIP6. *Atmospheric Chemistry and Physics*, *21*(17), 13571–13591.

Abalos, M., Orbe, C., Kinnison, D. E., Plummer, D., Oman, L. D., Jöckel, P., . . . others (2020). Future trends in stratosphere-to-troposphere transport in CCMI models. *Atmospheric Chemistry and Physics*, *20*(11), 6883–6901.

Abalos, M., Randel, W. J., Kinnison, D. E., & Garcia, R. R. (2017). Using the artificial tracer e90 to examine present and future UTLS tracer transport in WACCM. *Journal of the Atmospheric Sciences*, *74*(10), 3383–3403.

Andrews, D., Holton, J., & Leovy, C. (1987). Middle Atmosphere Dynamics. *Academic Press*, *60*, 489. doi: 10.1175/1520-0469(2003)060⟨0103: CEOOAL⟩2.0.CO;2

Arnold, N. P., Putman, W. M., & Freitas, S. R. (2020). Impact of resolution and parameterized convection on the diurnal cycle of precipitation in a global nonhydrostatic model. *Journal of the Meteorological Society of Japan. Ser. II*.

Boering, K. A., Wofsy, S., Daube, B., Schneider, H., Loewenstein, M., Podolske, J., & Conway, T. (1996). Stratospheric mean ages and transport rates from observations of carbon dioxide and nitrous oxide. *Science*, *274*(5291), 1340–1343.

Butchart, N., Cionni, I., Eyring, V., Shepherd, T., Waugh, D., Akiyoshi, H., . . . others (2010). Chemistry–climate model simulations of twenty-first century stratospheric climate and circulation changes. *Journal of Climate*, *23*(20), 5349–5374.

Chiodo, G., & Polvani, L. M. (2019). The response of the ozone layer to quadrupled CO2 concentrations: Implications for climate. *Journal of Climate*, *32*(22), 7629–7642.

Chou, M.-D. (1990). Parameterizations for the absorption of solar radiation by O2 and CO2 with application to climate studies. *Journal of Climate*, *3*(2), 209–217.

Chou, M.-D. (1992). A solar radiation model for use in climate studies. *Journal of Atmospheric Sciences*, *49*(9), 762–772.

Chou, M.-D., & Suarez, M. J. (1994). An efficient thermal infrared radiation parameterization for use in general circulation models.

Collow, A. B. M., Mahanama, S. P., Bosilovich, M. G., Koster, R. D., & Schubert, S. D. (2017). *An evaluation of teleconnections over the united states in an ensemble of AMIP simulations with the MERRA-2 configuration of the GEOS*

atmospheric model (Tech. Rep.).

Davis, N. A., Callaghan, P., Simpson, I. R., & Tilmes, S. (2022). Specified dynamics scheme impacts on wave-mean flow dynamics, convection, and tracer transport in CESM2 (WACCM6). *Atmospheric Chemistry and Physics*, *22*(1), 197–214.

Dietmüller, S., Eichinger, R., Garny, H., Birner, T., Boenisch, H., Pitari, G., . . . others (2018). Quantifying the effect of mixing on the mean age of air in CCMVal-2 and CCMI-1 models. *Atmospheric Chemistry and Physics*, *18*(9), 6699–6720.

Eichinger, R., Garny, H., Šácha, P., Danker, J., Dietmüller, S., & Oberländer-Hayn, S. (2020). Effects of missing gravity waves on stratospheric dynamics: Part 1, Climatology. *Climate Dynamics*, *54*(5), 3165–3183.

Eluszkiewicz, J., Hemler, R. S., Mahlman, J. D., Bruhwiler, L., & Takacs, L. L. (2000). Sensitivity of age-of-air calculations to the choice of advection scheme. *Journal of the Atmospheric Sciences*, *57*(19), 3185–3201.

Eyring, V., Lamarque, J.-F., Hess, P., Arfeuille, F., Bowman, K., Chipperfield, M. P., . . . others (2013). Overview of IGAC/SPARC Chemistry-Climate Model Initiative (CCMI) community simulations in support of upcoming ozone and climate assessments. *SPARC Newsletter*, *40*(January), 48–66.

Freitas, S. R., Grell, G. A., Molod, A., Thompson, M. A., Putman, W. M., Santos e Silva, C. M., & Souza, E. P. (2018). Assessing the Grell-Freitas convection parameterization in the NASA GEOS modeling system. *Journal of Advances in Modeling Earth Systems*, *10*(6), 1266–1289.

Freitas, S. R., Putman, W. M., Arnold, N. P., Adams, D. K., & Grell, G. A. (2020). Cascading toward a kilometer-scale GCM: Impacts of a scale-aware convection parameterization in the Goddard Earth Observing System GCM. *Geophysical Research Letters*, *47*(17), e2020GL087682.

Fujiwara, M., Manney, G. L., Gray, L. J., Wright, J. S., Tegtmeier, S., Ivanciu, I., & Pilch Kedzierski, R. (2022). Sparc reanalysis intercomparison project (s-rip) final report.

Gelaro, R., McCarty, W., Suárez, M. J., Todling, R., Molod, A., Takacs, L., . . . others (2017). The modern-era retrospective analysis for research and applications, version 2 (MERRA-2). *Journal of Climate*, *30*(14), 5419–5454.

Grell, G. A., & Freitas, S. R. (2014). A scale and aerosol aware stochastic convective parameterization for weather and air quality modeling. *Atmospheric Chemistry and Physics*, *14*(10), 5233–5250.

Grooß, J.-U., & Russell III, J. M. (2005). A stratospheric climatology for O 3, H2O, CH4, NOx, HCl and HF derived from HALOE measurements. *Atmospheric Chemistry and Physics*, *5*(10), 2797–2807.

Gupta, A., Gerber, E. P., & Lauritzen, P. H. (2020). Numerical impacts on tracer transport: A proposed intercomparison test of Atmospheric General Circulation Models. *Quarterly Journal of the Royal Meteorological Society*, *146*(733), 3937–3964.

Hall, T. M., & Plumb, R. A. (1994). Age as a diagnostic of stratospheric transport. *Journal of Geophysical Research: Atmospheres*, *99*(D1), 1059–1070.

Hall, T. M., Waugh, D. W., Boering, K. A., & Plumb, R. A. (1999). Evaluation of transport in stratospheric models. *Journal of Geophysical Research: Atmospheres*, *104*(D15), 18815–18839.

Hardiman, S. C., Butchart, N., & Calvo, N. (2014). The morphology of the Brewer–Dobson circulation and its response to climate change in CMIP5 simulations. *Quarterly Journal of the Royal Meteorological Society*, *140*(683), 1958–1965.

Haynes, P., McIntyre, M., Shepherd, T., Marks, C., & Shine, K. P. (1991). On the "downward control" of extratropical diabatic circulations by eddy-induced mean zonal forces. *Journal of the Atmospheric Sciences*, *48*(4), 651–678.

Hegglin, M. I., Brunner, D., Peter, T., Hoor, P., Fischer, H., Staehelin, J., . . . Weers, U. (2006). Measurements of NO, NOy, N2O, and O3 during SPURT: implica-

tions for transport and chemistry in the lowermost stratosphere. *Atmospheric Chemistry and Physics*, *6*(5), 1331–1350.

Holton, J. R., Haynes, P. H., McIntyre, M. E., Douglass, A. R., Rood, R. B., & Pfister, L. (1995). Stratosphere-troposphere exchange. *Reviews of Geophysics*, *33*(4), 403–439.

Holzer, M., & Hall, T. M. (2000). Transit-time and tracer-age distributions in geophysical flows. *Journal of the atmospheric sciences*, *57*(21), 3539–3558.

Iacono, M. J., Delamere, J. S., Mlawer, E. J., Shephard, M. W., Clough, S. A., & Collins, W. D. (2008). Radiative forcing by long-lived greenhouse gases: Calculations with the AER radiative transfer models. *Journal of Geophysical Research: Atmospheres*, *113*(D13).

Ivy, D. J., Solomon, S., Calvo, N., & Thompson, D. W. (2017). Observed connections of arctic stratospheric ozone extremes to Northern Hemisphere surface climate. *Environmental Research Letters*, *12*(2), 024004.

Kouatchou, J., Molod, A., Nielsen, J., Auer, B., Putman, W., & Clune, T. (2015). *GEOS-5 chemistry transport model user's guide* (Tech. Rep.).

Legras, B., Pisso, I., Berthet, G., & Lefèvre, F. (2004). Variability of the lagrangian turbulent diffusivity in the lower stratosphere. *Atmospheric Chemistry and Physics Discussions*, *4*(6), 8285–8325.

Lin, S.-J. (2004). A "vertically lagrangian" finite-volume dynamical core for global models. *Monthly Weather Review*, *132*(10), 2293–2307.

Molod, A., Takacs, L., Suarez, M., & Bacmeister, J. (2015). Development of the GEOS-5 atmospheric general circulation model: Evolution from MERRA to MERRA2. *Geoscientific Model Development*, *8*(5), 1339–1356.

Monge-Sanz, B., Chipperfield, M., Simmons, A., & Uppala, S. (2007). Mean age of air and transport in a CTM: Comparison of different ECMWF analyses. *Geophysical Research Letters*, *34*(4).

Monge-Sanz, B. M., Bozzo, A., Byrne, N., Chipperfield, M. P., Diamantakis, M., Flemming, J., . . . others (2022). A stratospheric prognostic ozone for seamless Earth system models: performance, impacts and future. *Atmospheric Chemistry and Physics*, *22*(7), 4277–4302.

Morgenstern, O., & Carver, G. D. (2001). Comparison of cross-tropopause transport and ozone in the upper troposphere and lower stratosphere region. *Journal of Geophysical Research: Atmospheres*, *106*(D10), 10205–10221.

Neu, J., Strahan, S., Braesicke, P., Douglass, A., Huck, P., Oman, L., . . . Tegtmeier, S. (2010). SPARC CCMVal (2010), SPARC Report on the Evaluation of Chemistry-Climate Models: Chapter 5: Transport. SPARC.

Neu, J. L., & Plumb, R. A. (1999). Age of air in a "leaky pipe" model of stratospheric transport. *Journal of Geophysical Research: Atmospheres*, *104*(D16), 19243–19255.

Oehrlein, J., Chiodo, G., & Polvani, L. M. (2020). The effect of interactive ozone chemistry on weak and strong stratospheric polar vortex events. *Atmospheric Chemistry and Physics*, *20*(17), 10531–10544.

Orbe, C., Oman, L. D., Strahan, S. E., Waugh, D. W., Pawson, S., Takacs, L. L., & Molod, A. M. (2017). Large-scale atmospheric transport in GEOS replay simulations. *Journal of Advances in Modeling Earth Systems*, *9*(7), 2545–2560.

Orbe, C., Rind, D., Jonas, J., Nazarenko, L., Faluvegi, G., Murray, L. T., . . . others (2020). GISS Model E2.2: A climate model optimized for the middle atmosphere—2. Validation of large-scale transport and evaluation of climate response. *Journal of Geophysical Research: Atmospheres*, *125*(24), e2020JD033151.

Orbe, C., Yang, H., Waugh, D. W., Zeng, G., Morgenstern, O., Kinnison, D. E., . . . others (2018). Large-scale tropospheric transport in the Chemistry–Climate Model Initiative (CCMI) simulations. *Atmospheric Chemistry and Physics*, *18*(10), 7217–7235.

Pan, L. L., Wei, J., Kinnison, D., Garcia, R., Wuebbles, D., & Brasseur, G. P. (2007). A set of diagnostics for evaluating chemistry-climate models in the extratropical tropopause region. *Journal of Geophysical Research: Atmospheres*, *112*(D9).

Pawson, S., Stajner, I., Kawa, S. R., Hayashi, H., Tan, W.-W., Nielsen, J. E., ... Livesey, N. J. (2007). Stratospheric transport using 6-h-averaged winds from a data assimilation system. *Journal of Geophysical Research: Atmospheres*, *112*(D23).

Plumb, R. A. (1985). On the three-dimensional propagation of stationary waves. *Journal of Atmospheric Sciences*, *42*(3), 217–229.

Plumb, R. A. (1996). A "tropical pipe" model of stratospheric transport. *Journal of Geophysical Research: Atmospheres*, *101*(D2), 3957–3972.

Plumb, R. A. (2002). Stratospheric transport. *Journal of the Meteorological Society of Japan. Ser. II*, *80*(4B), 793–809.

Polvani, L. M., Waugh, D. W., Correa, G. J., & Son, S.-W. (2011). Stratospheric ozone depletion: The main driver of twentieth-century atmospheric circulation changes in the southern hemisphere. *Journal of Climate*, *24*(3), 795–812.

Prather, M. J., Zhu, X., Tang, Q., Hsu, J., & Neu, J. L. (2011). An atmospheric chemist in search of the tropopause. *Journal of Geophysical Research: Atmospheres*, *116*(D4).

Rood, R. B. (1987). Numerical advection algorithms and their role in atmospheric transport and chemistry models. *Reviews of geophysics*, *25*(1), 71–100.

Rosenlof, K. H. (1995). Seasonal cycle of the residual mean meridional circulation in the stratosphere. *Journal of Geophysical Research: Atmospheres*, *100*(D3), 5173–5191.

Son, S.-W., Tandon, N. F., Polvani, L. M., & Waugh, D. W. (2009). Ozone hole and Southern Hemisphere climate change. *Geophysical Research Letters*, *36*(15).

Strahan, S., Douglass, A., & Newman, P. (2013). The contributions of chemistry and transport to low arctic ozone in March 2011 derived from aura MLS observations. *Journal of Geophysical Research: Atmospheres*, *118*(3), 1563–1576.

Thiele, G., & Sarmiento, J. (1990). Tracer dating and ocean ventilation. *Journal of Geophysical Research: Oceans*, *95*(C6), 9377–9391.

Waugh, D., & Hall, T. (2002). Age of stratospheric air: Theory, observations, and models. *Reviews of Geophysics*, *40*(4), 1–1.

Weaver, C. J., Douglass, A. R., & Rood, R. B. (1993). Thermodynamic balance of three-dimensional stratospheric winds derived from a data assimilation procedure. *Journal of Atmospheric Sciences*, *50*(17), 2987–2993.